Insight into the influence of alloying elements on the secondary corrosion protection of Fe-base alloys by means of atom probe tomography

Corrosion Science 235 (2024) 112175

Contents lists available at ScienceDirect

Corrosion Science

journal homepage: www.elsevier.com/locate/corsci

Insight into the influence of alloying elements on the secondary corrosion protection of Fe-base alloys by means of atom probe tomography

A. Persdotter [a,*], T. Boll [c,d], V. Ssenteza [b], T. Jonsson [b]

[a] Department of Industrial and Materials Science, Chalmers university of technology, SE-412 96, Sweden
[b] Department of Chemistry and Chemical engineering, Chalmers university of technology, SE-412 96, Sweden
[c] Institute for Applied Materials (IAM-WK), Karlsruhe Institute of Technology (KIT), Engelbert-Arnold-Str. 4, D-76131 Karlsruhe, Germany
[d] Karlsruhe Nano Micro Facility (KNMF), Karlsruhe Institute of Technology (KIT), Hermann-von-Helmholtz-Platz 1, D-76344 Eggenstein-Leopoldshafen, Germany

ARTICLE INFO

Keywords:
High temperature corrosion
APT
Breakaway oxidation
Secondary corrosion protection
Iron oxide
Spinel
FeCrAl
FeCrNi

ABSTRACT

Breakaway corrosion of Fe-base alloys remains a challenge in applications operated in harsh conditions. The material lifetimes are often determined by the corrosion propagation after breakaway. Nevertheless, detailed microstructural studies, linking the protective properties of the Fe-rich oxides formed after breakaway, are scarce. This study utilizes APT to investigate the Fe-rich oxides formed after breakaway, i.e., the secondary corrosion protection, of four Fe-based model alloys chosen to exhibit good and poor secondary protection at 600 °C. The APT investigation shows that the inward-growing scale is heterogeneous at the nanometer scale and that Fe-enriched regions form on the poorly protective oxides.

1. Introduction

High temperature corrosion remains a challenge in many industrial applications and is commonly addressed by using highly alloyed materials such as stainless steels or FeCrAl alloys. The corrosion protection of these materials rely on the formation of a protective Cr- and/or Al-rich corundum-type oxide [1,2], also known as the primary corrosion protection [3]. However, in harsh corrosive environments, these oxides tend to break down resulting in the formation of a fast-growing, Fe-rich oxide scale, a process known as breakaway corrosion [2,4–13]. The oxidation process after breakaway at high temperatures is significantly accelerated. However, both stainless steels and FeCrAl alloys may form a comparatively slow Fe-rich oxide scale after breakaway, i.e. a secondary corrosion protection, at intermediate temperatures (<700 °C).

In harsh corrosive environments, the oxides formed on the alloy surface often spall off. The ability to withstand spallation is an important property that has not been investigated in this study. However, if spallation is presumed to occur (applicable for many harsh environments) the oxidation rate, as investigated in this study, between each spallation event becomes increasingly important for the overall material lifetime. This is due to the fact that the overall oxidation kinetics for a process including frequently occurring spallation events (see Fig. 1) would be determined by the magnitude of each step in combination with the number of spallation events. Thus, the corrosion propagation after breakaway, and material lifetime, is determined by the materials ability to form a protective, slow-growing oxide scale after breakaway, i.e., a good secondary corrosion protection of the alloy [3]. Nevertheless, a large part of previous research has been focused on the initiation/breakaway, while less studies have focused on the performance after breakaway. In order to meet current, and future, corrosion challenges for applications operated in harsh conditions, the secondary corrosion protection, i.e., the protective properties of the multi-layered Fe-rich oxide scales, must be studied in further detail.

The selection of alloys and prediction of material lifetimes for applications operating in harsh conditions is at present based, to a large extent, on empirical knowledge. It has been shown that some alloys may sustain longer after breakaway than others (see e.g., [14–16]). However, the mechanistic understanding to the difference in corrosion rate is not completely understood and systematic studies on the growth mechanisms of the Fe-rich oxides formed on different alloys after breakaway are scarce. The scales formed after breakaway is experimentally challenging to investigate as the scales grows fast and may spall off. For this reason it is initially important to focus on shorter exposure times to limit the risk of spallation.

Recent studies have shown that the growth of the Fe-rich oxides formed after breakaway is often diffusion controlled, and may be significantly reduced by changing the alloy composition [3,15–17]. At intermediate temperatures (<700 °C) Fe-based alloys typically either form a fast-growing Fe-rich oxide with growth rates similar to

* Corresponding author.
E-mail address: amanda.persdotter@chalmers.se (A. Persdotter).

https://doi.org/10.1016/j.corsci.2024.112175
Received 1 March 2024; Received in revised form 13 May 2024; Accepted 1 June 2024
Available online 6 June 2024

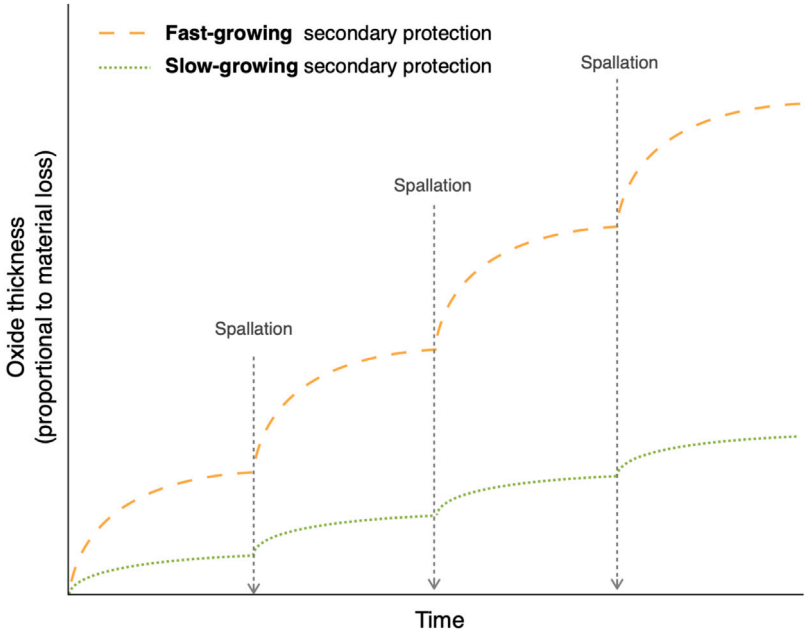

Fig. 1. Schematics illustrating the impact of different oxidation rates in applications dealing with re-occurring spallation events. The oxidation rate for each parabol becomes increasingly important for the overall material loss for higher spallation frequency occurs.

low alloyed steels (poor secondary protection), or slow-growing multi-layered Fe-rich oxide scales, with growth rates approximately one order of magnitude slower (good secondary corrosion protection) [18]. The results from investigations in several different corrosive environments indicate a similar microstructure after the onset of breakaway corrosion [5,6,9,19]. The Fe-rich oxide scales formed after breakaway are in general multi-layered, composed of an outward-growing pure Fe-oxide and an inward-growing mixed oxide scale. As the alloy composition is altered, the composition and microstructure of the inward growing scale is dramatically changed, whereas the outward-growing scales remain similar [3]. Thus, it has been proposed that the inward-growing scale is the most critical part in determining the corrosion protection after breakaway, i.e., the secondary corrosion protection.

The microstructure and chemical composition of the inward-growing oxide-scale, as partly formed through internal oxidation, is normally complex and porous. The composition and microstructure are expected to play a crucial role in the difference between a slow- and fast-growing secondary corrosion protection (i.e., the protection following the onset of breakaway corrosion). In particular, the outermost part of the inward-growing oxide (interface to the outward-growing scale) may be considered to be remnants of the first stage of the secondary corrosion protection (before the onset of internal oxidation). The properties of this part of the oxide scale may determine the corrosion propagation and following microstructure by influencing the kinetics for diffusion of species through the inward-growing oxide. Thus, this part of the oxide scale is of major interest to increase the understanding of the secondary corrosion protection of Fe-based alloys. The inward-growing scale has previously been investigated in detail by transmission electron microscopy ((S)TEM/EDX/EELS) [6,19]. However, to resolve the chemical composition of small regions (in the nanometer range) the 3D-influence of the thin foil analyzed in the TEM (approximately 100 nm thick) makes it difficult to fully interpret the results and understand the microstructure in detail.

This study aims to increase the understanding of the influence of alloying elements and corrosive species on the protective properties of the secondary corrosion protection, by utilizing the three-dimensional analysis of atom probe tomography (APT), in particular in the outermost region of the inward-growing scale. The study combines SEM/EDX with the high resolution and three-dimensional analysis of APT to investigate how the distribution of alloying elements within the inward-growing oxide scale may influence the protection against corrosive species such as chlorine and alkali and how these species interact with the oxides. The study investigates the oxide scales formed on four Fe-based model alloys chosen to exhibit good secondary corrosion protection, i.e., slow-growing oxides (Fe10Cr4Al2Si [20], Fe18Cr10Ni [3]), as well as poor secondary corrosion protection, i.e., fast-growing oxides (Fe10Cr4Al [20], Fe18Cr2Ni [3]). The oxides are thermally grown for 168 h at 600 °C in a corrosive environment containing 5%O_2 + 20%H_2O + 500 ppm HCl(g) + N_2(bal.) + 1 mg/cm^2 KCl(s).

Table 1
Nominal composition ([wt%] and [at%]) of the investigated Fe-based model alloys, representing alloys previously observed to form poor (Fe10Cr4Al, Fe18Cr2Ni) as well as good (Fe10Cr4Al2Si, Fe18Cr10Ni) secondary corrosion protection in the presence of KCl(s).

Alloy	Fe	Cr	Al	Si	Ni	Zr	Fe	Cr	Al	Si	Ni	Zr
Fe10Cr4Al	86	10	4	–	–	<0.3	82	10	8	–	–	<0.2
Fe10Cr4Al**2Si**	84	10	4	2	–	<0.3	78	10	8	4	–	<0.2
Fe18Cr**2Ni**	80	18	–	–	2	–	79	19	–	–	2	–
Fe18Cr**10Ni**	72	18	–	–	10	–	71	19	–	–	9	–
						wt%						at%

2. Experimental

In order to systematically study how the distribution of alloying elements within the inward-growing oxide scale may influence the secondary corrosion protection of Fe-based alloys, this study investigates the oxide scales formed on four Fe-based model alloys chosen to exhibit good (Fe10Cr4Al2Si, Fe18Cr10Ni) as well as poor (Fe10Cr4Al, Fe18Cr2Ni) secondary corrosion protection. The alloys were chosen to represent poor and good secondary corrosion protection in both the FeCrAl(Si)- and FeCrNi systems based on previous studies [3,15,20]. The nominal compositions of the investigated alloys are shown in Table 1.

Prior to exposures, sample coupons with dimensions 10 × 10x2 mm were ground with SiC (P500-P4000), Largo disc (9 μ mm) and polished with diamond suspension (3 and 1 μm). The polished coupons were degreased in acetone using ultrasonic agitation and finally cleaned with

ethanol. In order to study the secondary corrosion protection, all alloys were exposed in an environment known to rapidly induce breakaway corrosion [6,7]. The clean coupons were sprayed with a saturated solution of potassium chloride, KCl (1 mg/cm^2 KCl(s), dissolved in ethanol and water (80:20)). The samples were then isothermally exposed in a horizontal tube furnace for 168 h at 600 °C in 5% O_2+20% H_2O + 500 ppm HCl(g) + N_2(bal.). The gas flow through the system was set at 1000 ml/min. The samples were positioned parallel to the direction of the gas flow on an alumina sample holder. An alumina boat filled with KCl(s) was placed upstream the samples to reduce the rate of KCl evaporation from the sample surfaces during exposure.

To enable microstructural analysis of the oxide scales, cross sections were prepared by dry cutting and polishing (to a surface finish of 0.5 μm) with a Leica EM TXP and subsequent ion-milled in a Broad ion beam (BIB), using a Leica EM TIC 3X Ion beam milling system operated at 6 kV. Thin Si-wafers were attached to the samples surfaces prior to cutting, in order to protect the corrosion products. Samples for APT measurements were prepared using an FEI Versa3D LoVac DualBeam (for ROI-Pt-deposition) and an Auriga 60 DualBeam operated in high vacuum mode, using an in-situ lift-out procedure, with subsequent extraction and annular milling for final shaping of the tip.

The microstructure and composition of the oxide scales were investigated in cross-section by means of Scanning electron microscopy (SEM) and energy dispersive X-ray spectroscopy (EDX), using an FEI Quanta ESEM 200 as well as FEI Versa3D LoVac DualBeam, operated in high vacuum at 10–20 keV. Due to large errors associated with oxygen quantification in EDX analysis cationic percentages (at%) are reported, excluding oxygen, assuming stoichiometric oxides.

The APT measurements were performed on a Cameca Local Electrode Atom Probe (LEAP 4000X HR) at a set temperature of 60 K, a laser pulse energy of 30 pJ, an evaporation frequency of 100–200 kHz and a detection rate of 0.3–0.5%. The 3D atom maps were reconstructed based on SEM images and evaluated with IVAS 3.8.14. Oxygen was excluded in the reported quantification [at%] if not stated otherwise.

Thermodynamic calculations were carried out using the Thermo-Calc software [21] with database TCOX11. Note that the FeCrAl (and FeCrNi) phase diagrams were calculated with a total fixed amounts of Al (or Ni) for each region. Hence, the composition of each phase in the two- and three-phase regions cannot be extracted visually from the diagrams.

3. Results

The thicknesses and average compositions of the different layers of the oxide scales were analyzed by SEM/EDX. The analysis was made at an accelerating voltage of 20 keV, resulting in a large interaction volume and average composition of a comparatively large volume. The outward-growing iron oxide is dense and homogeneous, in contrast to the inward-growing scale. Thus, the average composition is supposed to be representative for the outward-growing, dense iron oxide, while, for the inward-growing scale, it represents an average composition of oxide regions of different compositions contained in a porous microstructure. The data was used to calculate the outward diffusion of iron, inward/outward ratios as well as to select representative regions for lift-out of APT samples.

Fig. 2 shows the total thicknesses of the oxides scales grown on the investigated FeCrAl(Si)/Ni alloys exposed for 168 h at 600 °C in a corrosive environment containing 5% O_2 + 20% H_2O + 500 ppm HCl(g) + N_2(bal.) + 1 mg/cm^2 KCl(s). Previous studies have shown that the incubation time to breakaway on both FeCrAl(Si) and FeCrNi alloys are short (see e.g. [3]). Thus, the oxide scale thicknesses measured in this study are considered to be good representations of the oxidation rates of the secondary protection following breakaway oxidation of these alloys. The results show that the growth rates of the oxide scales were significantly reduced as the amount of Si or Ni was increased on both the Fe10Cr4AlxSi-(x = 0, 2 wt%), and Fe18CrxNi (x = 2, 10 wt%) systems. Thus, the results clearly illustrate the poor- (fast-growing) and good- (slow-growing) secondary corrosion protection of FeCrAl(Si)/Ni alloys. The results are compared to previous studies [3,20], on oxide scales grown under similar exposure conditions, with lower/no chlorine (Eklund et al. [20]: 5%O_2+20%H_2O+N_2(bal.) + 1 mg/cm^2 KCl(s), and Persdotter et al. [3]: 5%O_2+N_2 + 1 mg/cm^2 K_2CO_3(s), see Fig. 2. The comparison illustrates that the oxides grown in higher chlorine conditions (KCl(s)+HCl(g)) in this study, grow at a higher rate in general, but that the trends of poor- and good secondary corrosion protection remain similar. The poor- and good secondary corrosion protection of the FeCrAl(Si)-alloys and FeCrNi-alloys are studied separately below in order to gain a more generic understanding of how the secondary corrosion protection of Fe-based alloys may be altered by varying the alloy composition.

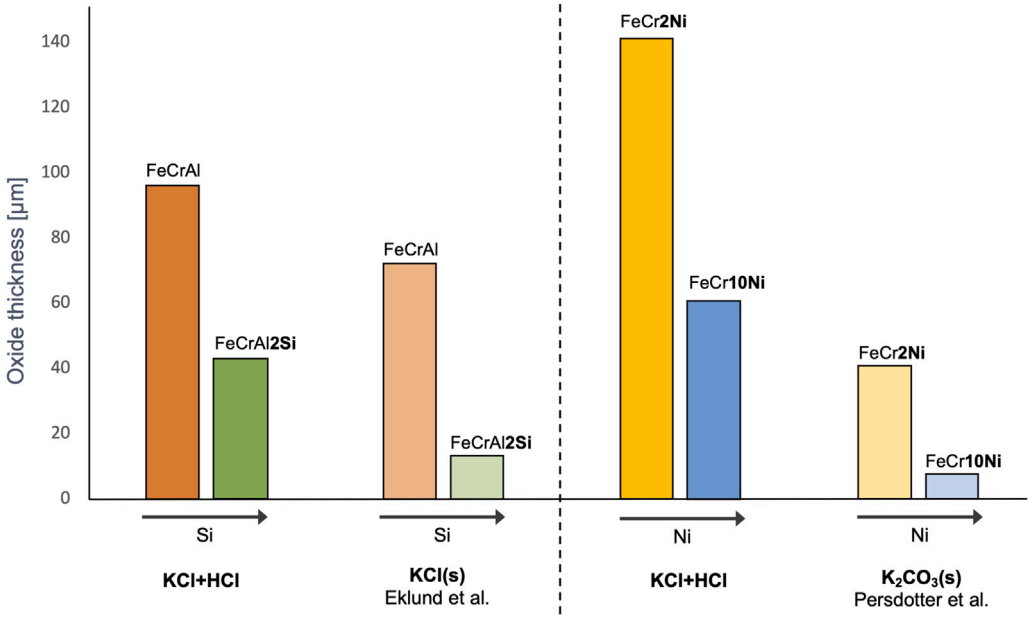

Fig. 2. Oxide thicknesses of FeCrAl(Si) and FeCrNi-alloys exposed for 168 h at 600 °C in a corrosive environment containing 5%O_2+20%H_2O+500 ppm HCl(g)+N_2(bal.) + 1 mg/cm^2 KCl(s). The results are compared to oxide thicknesses measured in previous studies exposed under similar, but less harsh conditions: Eklund et al. [20] (5%O_2+20%H_2O+N_2(bal.) + 1 mg/cm^2 KCl(s)) and Persdotter et al. [3] (5%O_2+N_2 + 1 mg/cm^2 K_2CO_3(s)).

3.1. Secondary corrosion protection of FeCrAl(Si)-alloys

The oxide scales formed on the FeCrAl(Si) alloys investigated are shown in Fig. 3 and characteristics of the microstructure is summarized in Table 2. The total oxide scale thickness was in average 95 μm on the Fe10Cr4Al alloy, and 37 μm on the Fe10Cr4Al2Si. The oxide scales were both composed of an outward-growing Fe-oxide, interpreted to consist of hematite (Fe_2O_3) on top of magnetite (Fe_3O_4), and an inward-growing oxide scale with a more complex microstructure and composition. The oxide grain sizes of both hematite and magnetite in the outward-growing scales were similar for the poorly protective Fe10Cr4Al alloy and the Fe10Cr4Al**2Si** alloy exhibiting a good secondary corrosion protection, see Table 2. The relative amounts (oxide thickness) of outward- and inward-growing scales were 62% outward-, and 38% inward-growing scale in the poorly protective oxide formed on Fe10Cr4Al. The oxide formed on the Fe10Cr4Al2Si alloy was composed of 73% outward- and 27% inward-growing scale. An internal oxidation zone (IOZ) was observed below the oxide scale formed on the Fe10Cr4Al alloy (see Fig. 3a), whereas the microstructure clearly implied a nitridation zone (NZ) in the same sample region on the Fe10Cr4Al**Si** alloy (see Fig. 3b). It should be noted that the inward-growing scale was porous and that Zr-particles were distributed throughout the inward-growing scales (see precipitates in bright contrast in Fig. 3, originating from the Zr-precipitates in the alloy).

The chemical composition of the inward-growing scale formed on the fast-growing FeCrAl-alloy (Fe10Cr4Al), as measured by SEM/EDX, was approximately 60 at% Fe, 20 at% Cr, and 20 at% Al (given in

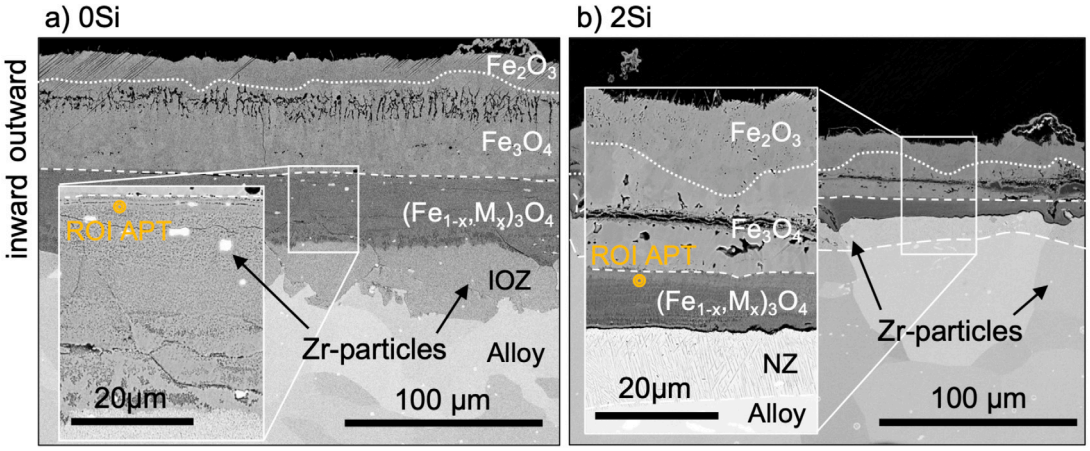

Fig. 3. BSE-SEM images of the oxide scales formed after 168 h of exposure of (a) the Fe10Cr4Al alloy exhibiting a poor secondary corrosion protection, and (b) Fe10Cr4Al**2Si** alloy exhibiting a good secondary corrosion protection. Inserted images show a selection of the inward-growing scale at higher magnification.

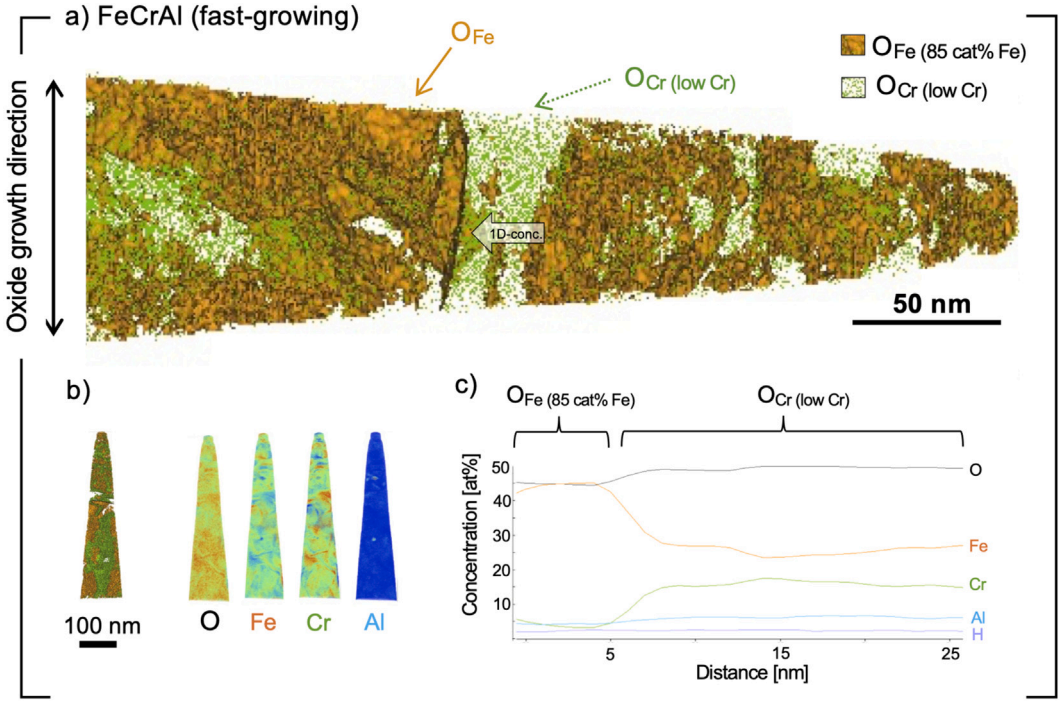

Fig. 4. (a) Reconstruction of APT-data showing the elemental distribution of the outermost part of the inward-growing oxide scale formed on Fe10Cr4Al(Zr) exposed at 600 °C for 168 h in the presence of 1 mg/cm^2 KCl(s) + 5% O_2+20% H_2O + 500 ppm HCl(g) + N_2(bal.), (see region of interest, ROI, in Fig. 3a). The orange isosurface represents an Fe-rich FeCrM-oxide (O_{Fe}: 85 cat%Fe), whereas the analyzed volume in between the isosurfaces illustrates the distribution of an FeCrM-oxide ($O_{Cr,\ (low\ Cr)}$) containing approximately 60 at% Fe and 30 at% Cr (reported for cations). For full composition see Table 3. (b) Heat maps showing the distribution of alloying elements in the APT specimen. Note that the heat maps show compositions relative to each separate element and should not be used to compare absolute concentrations. (c) 1D-concentration profile from region marked with arrow in Fig. 4a.

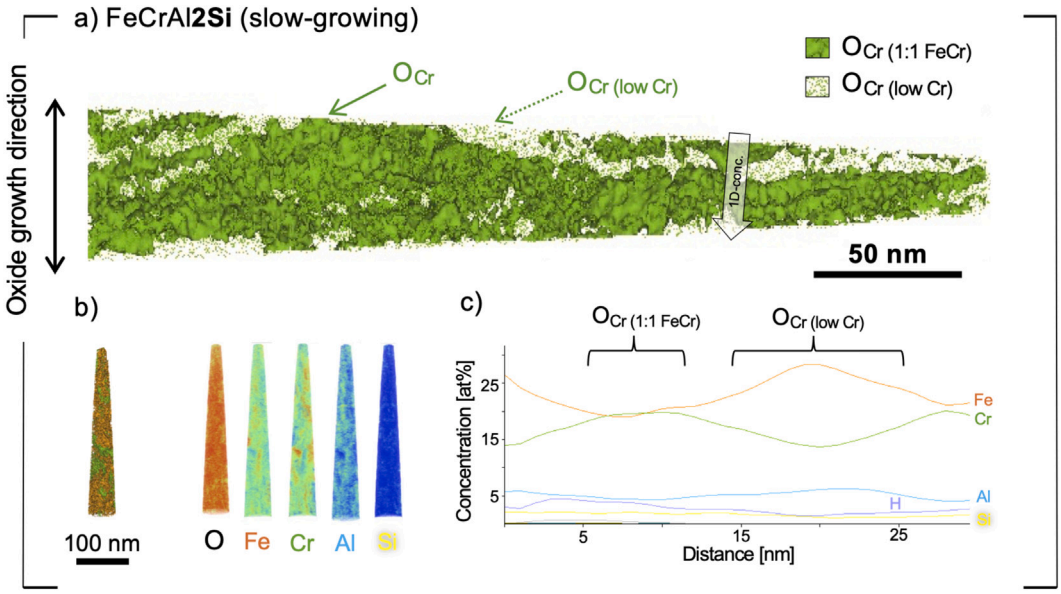

Fig. 5. (a) Reconstruction of APT-data showing the elemental distribution of the outermost part of the inward-growing oxide scale formed on Fe10Cr4Al2Si(Zr) exposed at 600 °C for 168 h in the presence of 1 mg/cm^2 KCl(s) + 5% O_2+20% H_2O + 500 ppm HCl(g) + N_2(bal.), (see region of interest, ROI, in Fig. 3b. The green isosurface represents an FeCrM-oxide (O_{Cr}(1:1, FeCr) composed of Fe and Cr at 1:1 relation, whereas the analyzed volume in between the isosurface illustrates the distribution of an FeCrM-oxide ($O_{Cr,\ (low\ Cr)}$) containing approximately 60 at% Fe and 30 at% Cr (reported for cations). See full composition in Table 3. (b) Heat maps showing the distribution of alloying elements in the APT specimen. Note that the heat maps show compositions relative to each separate element and should not be used to compare absolute concentrations. (c) 1D-concentration profile from region marked with arrow in Fig. 5a.

Table 2
Summary of oxide microstructure of multi-layered Fe-rich oxides formed on FeCrAl(Si) alloys after 168 h exposure at 600 °C in a corrosive environment containing 5%O_2+20%H_2O+500 ppm HCl(g)+N_2(bal.) + 1 mg/cm^2 KCl(s), including thickness of total oxide scale, inward-growing(in), and outward-growing(out) scale, internal oxidation zone (IOZ)/nitridation zone (NZ), and average grain sizes of hematite(Fe_2O_3) and magnetite(Fe_3O_4).

Alloy	Thickness [μm]							Grain size [μm]	
	Total	Out tot	Fe_2O_3	Fe_3O_4	In	IOZ/NZ	Out:In [%: %]	Fe_2O_3	Fe_3O_4
Fe10Cr4Al	95	59	13	46	36	33(IOZ)	62:38	0.2	1.7
Fe10Cr4Al**2Si**	37	27	8	19	10	12(NZ)	73:27	0.3	1.4

Table 3
Composition (at%, reported for cations), as measured by means of atom probe tomography, of oxides formed in the outermost part of the inward-growing scale formed on the investigated FeCrAl(Si) alloys exposed for 168 h at 600 °C in the presence of KCl(s) + 5% O_2+20% H_2O + 500 ppm HCl(g) + N_2(bal.). ROIs for APT-analysis are marked in Fig. 3.

	Oxide	Fe	Cr	Al	Si	[at% (cations)]
Fe10Cr4Al (fast-growing)	O_{Fe}	84	8	8	–	
	$O_{Cr,(low\ Cr)}$	60	29	11	–	
Fe10Cr4Al**2Si** (slow-growing)	$O_{Cr,\ 1:1,\ FeCr}$	44	44	9	3	
	$O_{Cr,\ (low\ Cr)}$	54	30	11	4	

cations). This represents a loss of only iron caused by outward diffusion to form the outward-growing iron oxide. The inward-growing scale formed on the FeCrAl(Si) alloy exhibiting a good secondary corrosion protection (Fe10Cr4Al**2Si**) contained approximately 40 at% Fe, 30 at% Cr, 20 at% Al, and 10 at% Si (given in cations). The compositions were again in good agreement with the unexposed alloys, after removal of Fe to grow the outward-growing scale. No significant amounts of chlorine or potassium were detected in the oxide scales or in the IOZ/NZ. Trace amounts of Cl (<<1%) were locally indicated in the EDX-spectrum, at the metal/oxide interface. However, the amounts detected were too low to quantify with certainty.

The outermost inward-growing oxide formed on the FeCrAl(Si) alloys represent the remains of the first stage of the secondary corrosion protection for both alloys (Fe10Cr4Al, Fe10Cr4Al**2Si**). The microstructure was investigated in detail (see region of interest (ROI) in Fig. 3a–b) by means of Atom probe tomography (APT) (see Figs. 4–5). The elemental distribution clearly demonstrated that the alloying elements were not homogeneously distributed in neither the sample exhibiting poor- nor good secondary corrosion protection. The oxides formed on the Fe10Cr4Al and Fe10Cr4Al2Si alloys were observed to be divided into regions with different composition as illustrated by the isosurfaces in Figs. 4 and 5. The isosurfaces represents regions of equal composition in the APT specimen used to visualize how the composition in the inward-growing spinel varies at the nanometer-length scales. The other alloying elements were also present in varying amounts in the oxide regions, as summarized in Table 3. The distribution of Al and Si are shown in the heat maps in Fig. 4b and 5b. Previous studies [3,9,10, 17,20,22] and thermodynamics suggest the oxides to be of spinel-type (O_{Fe} = S_{Fe} and O_{Cr} = S_{Cr}). However, the amounts of oxygen detected was significantly underestimated to approximately 50 at% (should be 57 at% for spinel, see discussion). The oxygen content remained similar for all O_{Cr}-regions, whereas a lower amount of oxygen was measured in the Fe-rich oxide regions(O_{Fe}). See 1D-concentration profiles in Fig. 4c.

The orange isosurface in Fig. 4a represents an Fe-rich FeCrM-oxide (O_{Fe}) containing 84 at% Fe, 8 at% Cr, 8 at% Al (given in cations), whereas the analyzed volumes in between the isosurfaces illustrate the distribution of an FeCrM-oxide ($O_{Cr,\ (low\ Cr)}$), containing approximately 60 at% Fe and 30 at% Cr (reported in cations), formed on both the FeCrAl(Si) alloys investigated. The average oxide compositions, as measured by APT, are summarized in Table 3 and were extracted

from proxigrams and 1D-concentration profiles (cross section ~15 nm) through the isosurfaces shown in Fig. 4.

The green isosurface in Fig. 5 represents the distribution of an FeCrM-oxide formed on the Fe10Cr4Al**2Si** alloy (O_{Cr}(1:1,FeCr)), composed of Fe and Cr at 1:1 relation. This oxide was composed of 44 at% Fe, 44 at% Cr, 9 at% Al, and 3 at% Si. The analyzed volume in between the isosurface illustrate the distribution of an FeCrM-oxide ($O_{Cr,\ (low\ Cr)}$), containing approximately 60 at% Fe and 30 at% Cr (reported in cations), formed on both FeCrAl(Si) alloys investigated. The average oxide compositions, as measured by APT, are summarized in Table 3 and were extracted from proxigrams and 1D-concentration profiles (cross section ~15 nm) through the isosurfaces shown in Figs. 4–5.

It may be noted that the APT-analysis did not reveal any Zr dispersed in the oxide in the analyzed region for any of the two investigated FeCrAl(Si)-Zr alloys, nor any detectable segregation of alloying elements or corrosive species (Cl or K) in e.g., grain boundaries. Trace amounts of chlorine (Cl) were indicated in the m/q spectrum in both the Fe10Cr4Al and Fe10Cr4Al**2Si** samples. However, a challenging overlap between $Cl/Cl_2/Cl_2H$ and FeO/FeOH/CrO makes the determination and quantification difficult. In addition, trace amounts of potassium(K) were indicated in the Fe10Cr4Al**2Si** sample. The potassium detected was homogeneously distributed throughout the whole APT-tip in similarity to the possible traces of Cl.

3.2. Secondary corrosion protection of FeCrNi-alloys

The oxide scales formed on the Fe18CrNi alloys are shown in Fig. 6 and summarized in Table 4. The total oxide scale thickness after 168 h of exposure was approximately 140 μm on the Fe18Cr2Ni alloy, exhibiting poor secondary corrosion protection, whereas the total thickness of the oxide scale formed on the Fe18Cr10Ni alloy was approximately 34 μm. Both oxide scales consisted of an outward-growing, almost pure, Fe-oxide scale, interpreted to be composed of hematite (Fe_2O_3) on top of magnetite (Fe_3O_4), see Table 4, and an inward-growing scale with a more complex microstructure and composition. The oxide grain sizes of both hematite and magnetite in the outward-growing scale were observed to be smaller on the Fe18Cr**10Ni** alloy, as compared to the poorly protective oxide formed on the Fe18Cr**2Ni** alloy (see Table 4). The relative amounts of outward- and inward-growing scales were 53% outward-, and 47% inward-growing scale in the poorly protective oxide formed on Fe18Cr2Ni, whereas the oxide formed on the Fe18Cr10Ni alloy was composed of 80% outward- and 20% inward-growing scale (see Table 4). An internal oxidation zone was clearly defined on both samples. The corrosion front was straight (i.e. homogeneous oxide growth over the sample surface) on the Fe18Cr2Ni, while it was observed to be more undulating on the Fe18Cr10Ni alloy, with faster growth at the alloy grain boundaries (see Fig. 6). This would be expected since the difference in bulk and grain boundary diffusion rate is larger for austenitic alloys (Fe18Cr10Ni) than for ferritic alloys (Fe18Cr2Ni). It may be noted that the internal oxidation zone on the Fe18Cr10Ni alloy is approximately the same thickness (depth, Table 4) inside the alloy grains as at the alloy grain boundaries (see Fig. 6b). By hypothetically "stretching" the corrosion front at the alloy grain boundaries, one may observe a rather homogeneous corrosion attack, more similar (but slower), to the corrosion attack on the ferritic Fe18Cr**2Ni**. This indicates that the conditions at the corrosion front are similar for both the FeCrNi alloys.

The inward-growing scales were porous and contained Ni-rich metallic regions (see precipitates with brighter contrast in Fig. 6). The exact composition of the metallic Ni-rich precipitates could not be quantified by means of SEM/EDX since the precipitates were smaller than the size of the electron interaction volume. However, qualitatively the EDX-revealed Ni-enrichment in these regions and the brighter BSE contrast in Fig. 6 strongly suggests that the regions are metallic. It may be noted that the Ni-rich metallic regions were larger in size on the Fe18Cr10Ni alloy (see Fig. 6b), in particular at the alloy grain boundaries, where the oxide was also observed to be locally denser. The composition of the inward-growing scale formed on the Fe18Cr2Ni alloy (representing a poor secondary corrosion protection) was measured by means of SEM/EDX. The inward-growing scale was in average composed of 56 at% Fe, 42 at% Cr, and 3 at% Ni (given in cations), in good agreement with the composition of the unexposed alloy, after removal of Fe to grow the outward-growing scale. The inward-growing scale formed on the Fe18Cr10Ni alloy (representing a good secondary corrosion protection) was not measured by means of SEM/EDX, due to unfortunate spallation of the scale.

The outermost inward-growing oxides formed on the FeCrNi alloys (see region of interest (ROI) in Fig. 6a–b) were analyzed using the same strategy as for the FeCrAl(Si) alloys, i.e., by means of APT. The results showed that the elemental distributions of the analyzed oxide regions were clearly heterogeneous, which can be seen in Figs. 7 and 8. The composition (Fe, Cr and Ni) of each oxide region is summarized in Table 5. The oxide formed on the Fe18Cr2Ni alloy was separated into two regions; (i): an Fe-rich FeCrM-oxide (O_{Fe}), represented by the elongated (10–20 nm width) orange isosurface in Fig. 7a, and (ii): an FeCr-rich oxide (O_{Cr}(1:1, FeCr)), exhibiting a 1:1 relation in Fe:Cr content. The Fe-rich oxide (O_{Fe}) was composed of approximately 84 at% Fe, 9 at %Cr, and 7 at%Ni (given in cations), whereas the other FeCrM-oxide (O_{Fe}(1:1, FeCr)) was composed of approximately 49 at% Fe, 49 at % Cr, and 2 at% Ni (given in cations). The compositions of

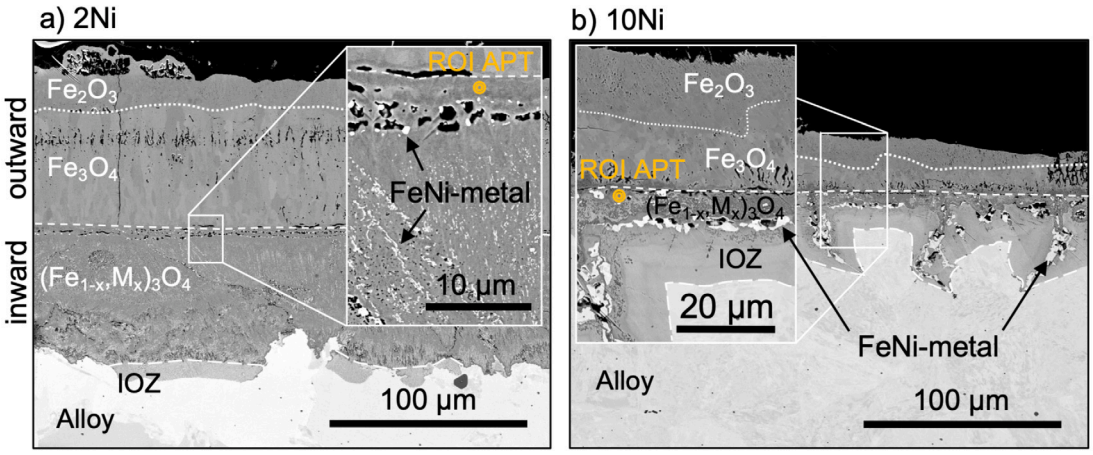

Fig. 6. BSE-SEM images of the oxide scales formed after 168 h of exposure of (a) the Fe18Cr2Ni alloy exhibiting a poor secondary corrosion protection, and (b) Fe18Cr10Ni alloy exhibiting a good secondary corrosion protection. Inserted images show a selection of the inward-growing scale at higher magnification.

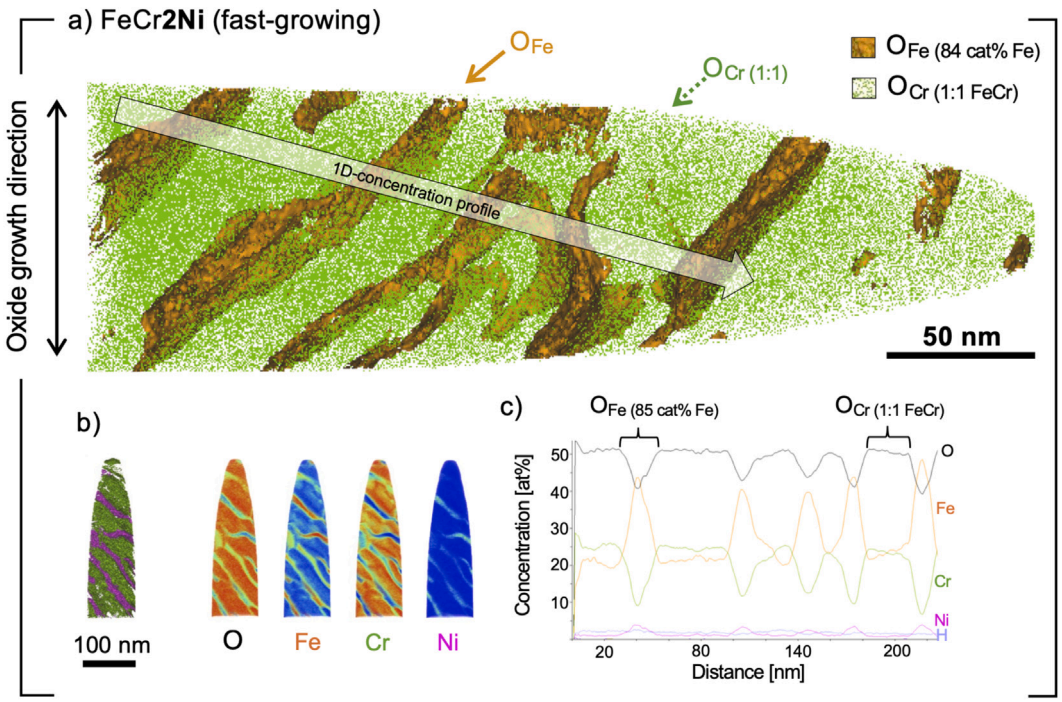

Fig. 7. (a) Reconstruction of APT data showing the elemental distribution of the outermost part of the inward-growing oxide scale formed on Fe18Cr2Ni exposed at 600 °C for 168 h in the presence of 1 mg/cm^2 KCl(s) + 5% O_2+20% H_2O + 500 ppm HCl(g) + N_2(bal.), (see region of interest, ROI, in Fig. 6a). The orange isosurface represents an Fe-rich FeCrM-oxide (O_{Fe}: 84 cat% Fe), whereas the analyzed volume in between the isosurface illustrates the distribution of an FeCrM-oxide (O_{Cr}(1:1, FeCr)), composed of Fe and Cr at 1:1 relation. For full composition see Table 5. (b) Heat maps showing the distribution of alloying elements in the APT specimen. Note that the heat maps show compositions relative to each separate element and should not be used to compare absolute concentrations. (c) 1D-concentration profile from region marked with arrow in Fig. 7a.

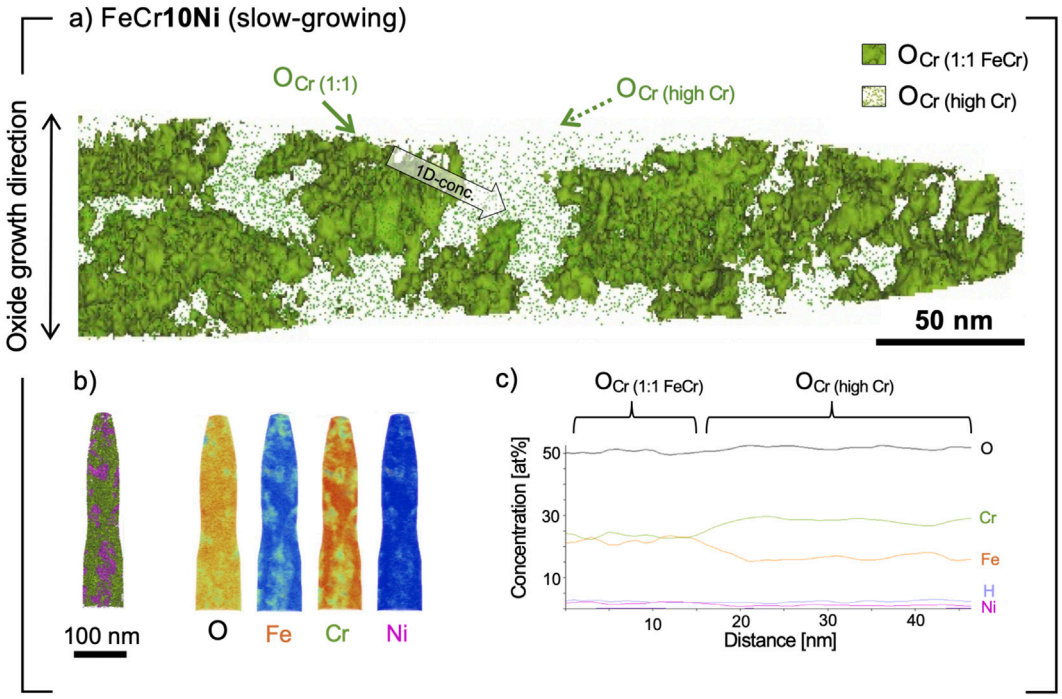

Fig. 8. (a) Reconstructions of APT data showing the elemental distribution of the outermost part of the inward-growing oxide scale formed on Fe18Cr10Ni exposed at 600 °C for 168 h in the presence of 1 mg/cm^2 KCl(s) + 5% O_2+20% H_2O + 500 ppm HCl(g) + N_2(bal.), (see region of interest, ROI, in Fig. 6b). The green isosurface represents an FeCrM-oxide (O_{Cr}(1:1, FeCr)), composed of Fe and Cr at 1:1 relation, whereas the analyzed volume in between the isosurfaces illustrates the distribution of a Cr-rich FeCrM-oxide (O_{Cr}(high Cr)), containing approximately 60 at% Fe and 30 at% Cr (reported for cations). For full composition see Table 5. (b) Heat maps showing the distribution of alloying elements in the APT specimen. Note that the heat maps show compositions relative to each separate element and should not be used to compare absolute concentrations. (c) 1D-concentration profile from region marked with arrow in Fig. 8a.

the different oxide regions are reported in Table 5. The reported compositions are extracted averages from 1D-concentration profiles and proxigrams through the isosurfaces in Figs. 7 and 8. The oxygen content remained similar for all O_{Cr}-regions, significantly underestimated to 50

Table 4
Summary of oxide microstructure of multi-layered Fe-rich oxides formed on FeCrNi alloys after 168 h exposure at 600 °C in a corrosive environment containing 5%O_2+20%H_2O+500 ppm HCl(g)+N_2(bal.) + 1 mg/cm^2 KCl(s), including thickness of total oxide scale, inward-growing(in), and outward-growing(out) scale, internal oxidation zone (IOZ) and average grain sizes of hematite(Fe_2O_3) and magnetite(Fe_3O_4).

Alloy	Thickness	[μm]						Grain size	[μm]
	Total	Out tot	Fe_2O_3	Fe_3O_4	In	IOZ	Out:In [%: %]	Fe_2O_3	Fe_3O_4
Fe18Cr**2Ni**	141	75	13	62	66	8	53:47	0.5	1.5-3
Fe18Cr**10Ni**	34	27	10	17	7	11	80:20	0.2	1-2

Table 5
Composition (at%, given in cations), as measured by means of atom probe tomography, of oxides formed in the outermost part of the inward-growing scale formed on the investigated FeCrNi alloys exposed for 168 h at 600 °C in the presence of KCl(s) + 5% O_2+20% H_2O + 500 ppm HCl(g) + N_2(bal.). ROI for APT-analysis is marked in Fig. 6.

	Oxide	Fe	Cr	Ni	[at% (cations)]
Fe18Cr**2Ni** (fast-growing)	O_{Fe}	84	9	7	–
	$O_{Cr,1:1,\ FeCr}$	49	49	2	
Fe18Cr**10Ni** (slow-growing)	$O_{Cr,1:1,\ FeCr}$	48	48	4	
	$O_{Cr,(high\ Cr)}$	35	62	2	

at%, whereas a lower amount of oxygen (~40 at%) was measured in the Fe-rich oxide regions(O_{Fe}), in similarity to the FeCrAl-alloy (see 1D-concentration profile in Fig. 7.

The analyzed region of the inward-growing oxide representing a good secondary corrosion protection (Fe18Cr10Ni) was also separated into two FeCrM-oxide regions, with varying Cr-contents (O_{Cr}(1:1, FeCr) and O_{Cr}(high)), see Fig. 8. The oxide containing the least amount of Cr (O_{Cr}(1:1)), visualized by the green isosurface in Fig. 8a, was composed of approximately 48 at%Fe, 48 at% Cr, and 4 at%Ni (given in cations), while the oxide containing the highest amount of Cr, O_{Cr}(high Cr), was composed of approximately 35 at%Fe, 62 at%Cr, and 2 at%Ni (given in cations). In similarity to the oxides formed on the FeCrAl(Si) alloys, the APT analysis revealed no specific segregation of alloying elements nor corrosive species (Cl or K) to grain boundaries. Trace amounts of chlorine (<0.1 at%) were indicated throughout the APT-tip on both the FeCrNi alloys. However, the challenging overlaps of Cl/Cl_2/Cl_2H and FeO/FeOH/CrO makes it difficult to conclude the presence and amount with certainty. The distribution of the possible trace amounts of chlorine suggests no obvious segregation to any interfaces or specific regions. No indications of potassium were observed in the analyzed region for neither of the FeCrNi alloys.

4. Discussion

This study investigates in detail the oxide scales formed after breakaway at 600 °C to increase the understanding of the possibilities to alter the protective properties of the iron-rich oxide scales formed after breakaway by changing the alloy composition. The microstructural investigation performed indicate a diffusion-controlled growth mechanism after breakaway despite the presence of chlorine (see Figs. 3 and 6). The microstructures were similar to the oxide scales observed in previous studies performed in several different corrosive environments [5,6,9,19]. All alloys investigated formed multi-layered Fe-rich oxide scales after breakaway with significantly reduced growth rates for higher Si (FeCrAl(Si)) or Ni (FeCrNi) contents, indicating an improved secondary corrosion protection (i.e., protection exerted by the multi-layered Fe-rich oxide scale [3]). The results clearly demonstrated that the alloys previously observed to form a good secondary protection in the presence of KCl or K_2CO_3 [3,20] remained the most protective also under high chlorine loads (KCl+HCl), indicating a versatile secondary corrosion protection at intermediate temperatures (see Fig. 2).

Internal oxidation was observed below the oxide scales on all alloys except for the Fe10Cr4Al**Si** alloy, on which the microstructure clearly implied nitridation (see Fig. 3b). Nitridation is well known to negatively effect the primary corrosion protection of FeCrAl alloys. This is due to the fact that aluminum nitrides holds aluminum, hindering the formation of a protective alumina scale at the metal/oxide interface. However, the secondary corrosion protection is not dependent on the formation of an alumina layer. Thus, the secondary corrosion protection of FeCrAl alloys is assumed to be unaffected by the nitridation, as indicated in this and several previous studies [15,23].

The total thickness of the outward-growing hematite (obtaining the highest grain boundary density of the outward-growing scale) was observed to be similar for all the investigated alloys. The oxide grain sizes of the outward-growing hematite (Fe_2O_3) and magnetite (Fe_3O_4) were also similar for alloys forming poor and good secondary corrosion protection, even though slightly larger oxide grains were observed on the Fe18Cr2Ni (see Table 4). Thus, the difference in growth rate after breakaway may not be explained by microstructural changes in the outward-growing scale. This is in line with earlier observations on the secondary corrosion protection [3]. The alloys exhibiting a good secondary corrosion protection form both thinner inward- as well as outward-growing scales, which may indicate that the inward-growing scale formed on the alloys exhibiting a good secondary corrosion protection slows down the supply of Fe to the outward-growing scale. Thus, it is proposed that the composition and structure of the inward-growing scale determines the corrosion resistance of the alloy after the onset of breakaway. This implies that the addition of alloying elements can improve the secondary corrosion protection (i.e., protection of Fe-rich oxide scale), however with different mechanisms compared to the corrosion resistance before breakaway, i.e., the primary corrosion protection.

The results from this study clearly demonstrate the potential in using APT analysis for investigating the complex inward-growing scale. The distribution of alloying elements in the outermost part of the inward-growing scale may appear homogeneous by characterization techniques such as STEM/EDX. However, from the APT results it is obvious that the alloying elements within the inward-growing oxides are not homogeneously distributed. The elemental distribution revealed a distinct separation in all inward-growing oxide scales, illustrated by the distribution of the main elements Fe and Cr in Figs. 4–8. This is in good agreement with a previous APT study performed on the spinel formed on a stainless steel (253 MA exposed at 970 °C) [22]. The other main alloying elements (Al, Si and Ni) were also present in various amounts separated between the oxide regions as shown in the heat maps in Figs. 4–8, and reported in Tables 3 and 5. The oxygen content remained similar for all O_{Cr}-regions, significantly underestimated to 45–50 at% (should be approximately 57 at% O for a spinel oxide), whereas the amounts measured in the Fe-rich oxide regions (O_{Fe}) were lower, 40–45 at%O, for both the FeCrAl and FeCrNi alloys exhibiting poor secondary protection. Note that a change in evaporation field between the oxide regions could result in lower oxygen. However, in this study, the ion density remained similar in both oxide regions, indicating no sharp change in evaporation field. The underestimation of oxygen has previously been reported for APT-analysis of iron oxides and have been systematically studied, suggesting that the underestimation is caused by a combination of multiple hits, dissociation of molecular ions as well as neutrals [24]. Due to the obvious underestimation, the oxygen contents reported in this study should not be interpreted as

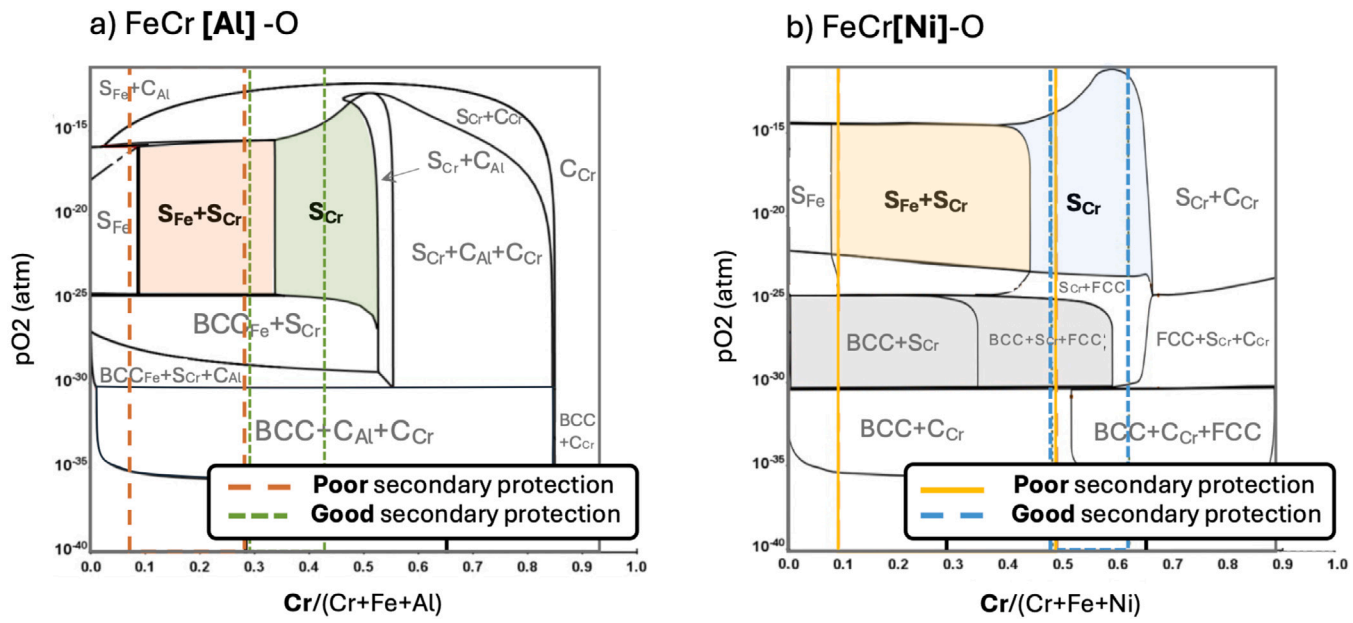

Fig. 9. Phase diagrams calculated using Thermo Calc [21] at 600 °C with fixed amounts of (a) Al(6 at%): FeCr[6at%Al]O-system), and (b) Ni(2 at%): FeCr[2at%Ni]O-system. The Cr content, as measured by APT in the outer part of the inward-growing spinel, are marked in the figure for the poor secondary protection (Fe10Cr4Al, Fe18Cr2Ni) and good secondary protection (Fe10Cr4Al2Si, Fe18Cr10Ni), clearly showing the tendency for spinel-phase separation in the alloys exhibiting poor secondary protection.

absolute numbers. Oxides are assumed stoichiometric and the cationic percentages are considered more accurate, hence tables report only cationic percent (cat%). The poorly protective mixed (FeCrM, M = Ni, Al and/or Si) oxides were distinctly separated in compositions consisting of an Fe-rich oxide (O_{Fe}) and a Cr-rich oxide (O_{Cr}). The good secondary corrosion protection were composed of only Cr-rich oxides (O_{Cr}), separated between low Cr(29–35 at% Cr), and intermediate Cr (1:1, 44–48 at% Cr) or high Cr (62 at% Cr) contents. Note that the oxides also contained various amounts of Al, Si, or Ni, as reported in Tables 3 and 5. Previous studies, in combination with thermodynamics, suggest that the oxides are mixed spinel-oxides [6,15,17,19,25], see Fig. 9: $O_{Fe} = S_{Fe}$, $O_{Cr} = S_{Cr}$).

The separation in composition may be closely linked to the thermodynamically predicted compositions of spinel at the corrosion front at 600 °C, as illustrated in the FeCr[Al/Ni]O-phase diagrams in Fig. 9. The alloys exhibiting poor secondary corrosion protection have cationic compositions that agree with the spinel phases S_{Fe}+S_{Cr} in the two-phase regions, whereas the compositions of the alloys exhibiting good secondary corrosion protection agree with the single phase spinel region (S_{Cr}). The phase diagrams are chosen for one fixed amount of Al and Ni respectively, to illustrate the spinel-miscibility gap. Note however that the range of stability for the single phase (S_{Cr}) and two-phase (S_{Fe}+S_{Cr}) spinel regions (as well as the internal oxidation region) are shifted at higher Al and/or Ni contents, resulting in even better agreement with the compositions measured (see eg., Eklund et al. [17] for the FeCrAlO-system, and [26] for the FeCrNiO-system). The clear separation in oxide composition between poor and good secondary protection (well predicted by the different stability regions in the phase diagrams) indicate that the miscibility gap between an Fe-rich and Cr-rich spinel could be related to the alloys ability to form a good secondary corrosion protection. Even though the miscibility gap is thermodynamically predicted, most previous studies performed at 600 °C [13,15,19,25] have not been able to observe a clear separation between Fe-rich and Cr-rich spinel in the inward-growing scale. This may be kinetically explained by that the slow diffusivity of Cr in spinel would impede the separation for longer diffusion lengths. However, at the nano-scale, the separation may take place (short distance for diffusion), which indeed is observed in the APT investigation in this study.

The difference in chemical composition between the good and poor secondary corrosion protection may in addition be complemented with the microstructure assessed by the three-dimensional capabilities of APT. The inward-growing spinel formed on both the protective scales (Fe10Cr4Al**2Si** and Fe18Cr**10Ni**) were observed to contain small regions of different composition that appeared not to be connected in the oxide growth direction, i.e., the diffusion path of oxygen/metal (see green isosurfaces in Figs. 5 and 8. However, the distribution of Fe-rich oxide (O_{Fe}) in the alloys exhibiting poor secondary corrosion protection (Fe10Cr4Al, Fe18Cr**2Ni**) indicated connected channels in the oxide growth direction in the outermost part of the inward-growing scale, in particular on the Fe18Cr**2Ni** alloy (see orange isosurfaces in Fig. 4a-7a). Note, that the volumes analyzed by APT are extremely small and that the indication of connected channels would require more statistics to conclude with certainty. Previous studies on the secondary corrosion protection (TEM) of FeCrAl(Si) alloys [15,17] indicated small sub-domains (a few nanometers in size) with different orientations, speculated to be nano-sized subgrains. The size of these domains agree with the 2D-projection (from certain angles) of the regions separated in composition as observed by means of APT in this study (see Figs. 4–8). Thus, it is possible that the indicated sub-domains are in fact oxide regions of different composition, which would be difficult to distinguish with characterization tools such as TEM.

If the Fe-rich oxide regions are connected they are probable to also be more accessible to corrosive species. However, the results from this study implied that no corrosive species (K or Cl) specifically segregated to any interfaces in the analyzed oxide. Nevertheless, the analyzed volumes in APT-studies are small, meaning that conclusive determinations of the distribution of corrosive species or alloying elements are difficult. In addition, the overlapping peaks in the m/q spectrum are challenging in the systems investigated. Thus, to further investigate the secondary corrosion protection of FeCrAl(Si)/Ni alloys, it is suggested to perform more STEM/EDX and/or APT investigations of the inward-growing scales formed on Fe-based alloys after breakaway.

Recent studies [15,26] have assigned the process of detrimental internal oxidation (S_{Cr}+BCC_{Fe} (+($FCC_{Fe,Ni}$)) and formation of rapidly consumed Fe-rich BCC metal (BCC_{Fe}), to the poor secondary corrosion protection observed on FeCrAl and FeCrNi alloys with certain compositions. It is reasonable to assume that the Fe-rich oxide regions, confined

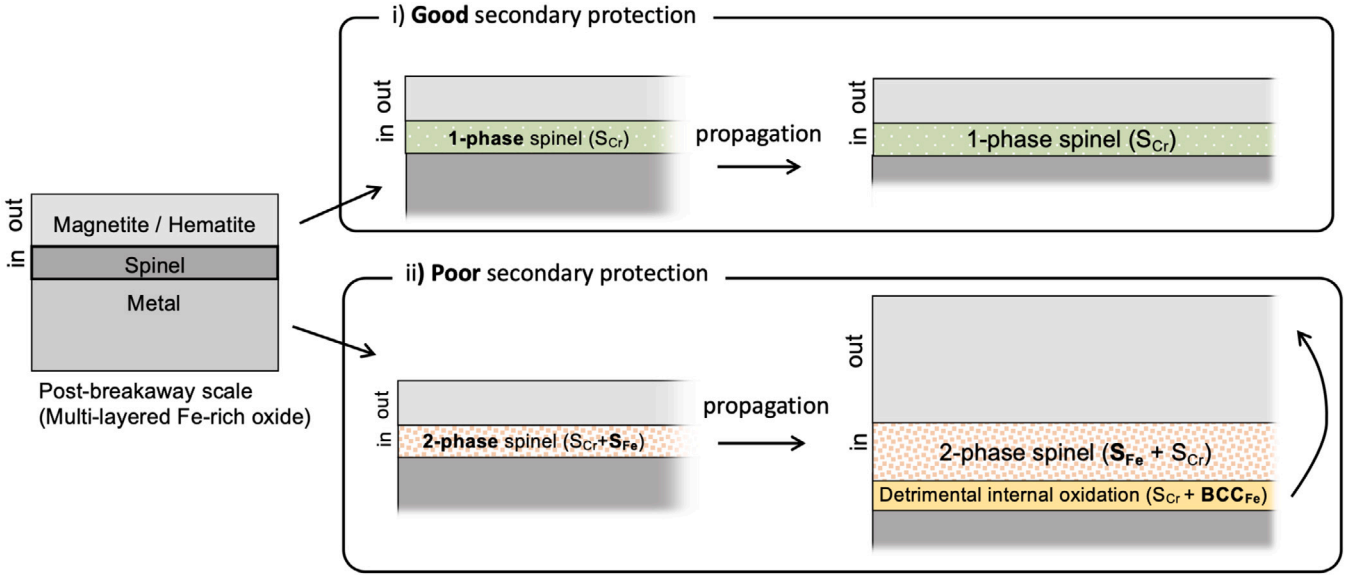

Fig. 10. Schematics illustrating the two pathways of oxide growth after breakaway (poor and good secondary corrosion protection).

in the outermost part of the inward-growing scale in this study, may play an important role in setting the conditions for (and composition of) the underlying oxide, consequently determining whether or not detrimental internal oxidation takes place (see schematics in Fig. 10). The alloys exhibiting good secondary corrosion protection were not observed to form Fe-rich oxide regions and were observed to avoid detrimental internal oxidation, which is suggested to explain the slower diffusion and more protective behavior.

5. Conclusion

The results in this study clearly demonstrate that the FeCrAl(Si)/(FeCrNi) alloys that form a good secondary protection in the presence of KCl (or K_2CO_3) also shows the same trend under high chlorine loads (KCl+HCl), indicating a versatile secondary corrosion protection. All alloys investigated formed multi-layered Fe-rich oxide scales after breakaway with significantly reduced growth rates for higher Si or Ni contents. The results suggest that the performance after breakaway is determined by the protective properties of the inward-growing oxide scale. The distribution of alloying elements, as measured by APT, elucidates the heterogeneous structure of the inward-growing oxide scale at the nanometer length scale. The inward-growing scale formed on the alloys exhibiting both poor-, and good secondary corrosion protection contained oxides with distinct separation in composition. Thus, it is proposed that the miscibility gap between Fe-rich and Cr-rich spinel as observed in the FeCr(Al/Ni)-O phase diagram is closely related the alloys performance after breakaway.

CRediT authorship contribution statement

A. Persdotter: Writing – review & editing, Writing – original draft, Visualization, Validation, Project administration, Methodology, Investigation, Formal analysis, Data curation, Conceptualization. **T. Boll:** Writing – review & editing, Validation, Supervision, Project administration, Methodology, Data curation. **V. Ssenteza:** Writing – review & editing, Methodology, Data curation. **T. Jonsson:** Writing – review & editing, Supervision, Conceptualization.

Declaration of competing interest

The authors declare that they have no known competing financial interests or personal relationships that could have appeared to influence the work reported in this paper.

Data availability

The raw/processed data required to reproduce these findings cannot be shared at this time as the data also forms part of an ongoing study.

Acknowledgments

This work was carried out within the Swedish High Temperature Corrosion Centre (HTC) at Chalmers University of Technology and the Karlsruhe nano micro facility (knmf) at Karlsruhe Institute of technology (KIT, no. 2023-030-031703), that are hereby gratefully acknowledged together with the Chalmers Materials Analysis Laboratory. The authors also acknowledges Delphine Chassaing, KIT, for APT-sample preparation, as well as Sedi Bigdeli, Höganäs AB, and Henrik Larsson, KTH, for performing thermodynamic calculations.

References

[1] P. Kofstad, High Temperature Corrosion, Elsevier Applied Science, London/New York, 1988.
[2] D.J. Young, High Temperature Oxidation and Corrosion of Metals, second ed., Elsevier, 2016.
[3] A. Persdotter, J. Eklund, J. Liske, T. Jonsson, Beyond breakaway corrosion - Influence of chromium, nickel and aluminum on corrosion of iron-based alloys at 600 °C, Corros. Sci. (March) (2020).
[4] G.C. Wood, D.P. Whittle, The mechanism of breakthrough of protective chromium oxide scales on Fe-Cr alloys, Corros. Sci. 7 (11) (1967).
[5] T. Gheno, D. Monceau, D.J. Young, Mechanism of breakaway oxidation of Fe – Cr and Fe – Cr – Ni alloys in dry and wet carbon dioxide, Corros. Sci. 64 (2012) 222–233.
[6] T. Jonsson, S. Karlsson, H. Hooshyar, M. Sattari, J. Liske, J.-E. Svensson, L.-G. Johansson, Oxidation after breakdown of the chromium-rich scale on stainless steels at high temperature : Internal oxidation, Oxidat. Met. 85 (2016) 509–536.
[7] J. Pettersson, J.-E. Svensson, L.-G. Johansson, Alkali induced corrosion of 304-type austenitic stainless steel at 600 °C; comparison between KCl, K_2CO_3 and K_2SO_4, Mater. Sci. Forum 595-598 PA (2008) 367–375.
[8] A. Col, V. Parry, C. Pascal, Oxidation of a Fe–18Cr–8Ni austenitic stainless steel at 850 °C in O_2: Microstructure evolution during breakaway oxidation, Corros. Sci. 114 (2017) 17–27.
[9] R. Peraldi, B.A. Pint, Effect of Cr and Ni contents on the oxidation behavior of ferritic and austenitic model alloys in air with water vapor, Oxidat. Met. 61 (5–6) (2004) 463–483.
[10] B. Pujilaksono, T. Jonsson, H. Heidari, M. Halvarsson, J.E. Svensson, L.G. Johansson, Oxidation of binary FeCr alloys (Fe-2.25Cr, Fe-10Cr, Fe-18Cr and Fe-25Cr) in O_2 and in O_2 + H_2O environment at 600 °C, Oxidat. Met. 75 (3–4) (2011) 183–207.
[11] N.K. Othman, J. Zhang, D.J. Young, Water vapour effects on Fe-Cr alloy oxidation, Oxidat. Met. 73 (1–2) (2010) 337–352.

[12] E. Essuman, G.H. Meier, J. Zurek, M. Hänsel, L. Singheiser, W.J. Quadakkers, Enhanced internal oxidation as trigger for breakaway oxidation of Fe-Cr alloys in gases containing water vapor, Scr. Mater. 57 (9) (2007) 845–848.
[13] T. Jonsson, H. Larsson, S. Karlsson, H. Hooshyar, M. Sattari, J. Liske, J.E. Svensson, L.G. Johansson, High-temperature oxidation of FeCr(Ni) alloys: The behaviour after breakaway, Oxidat. Met. 87 (3–4) (2017) 333–341.
[14] J. Eklund, M.D. Paz, B. Jönsson, J. Liske, J.E. Svensson, T. Jonsson, Field exposure of FeCrAl model alloys in a waste-fired boiler at 600 °C: The influence of Cr and Si on the corrosion behaviour, Mater. Corros. 70 (8) (2019) 1476–1485.
[15] J. Eklund, A. Persdotter, V. Ssenteza, T. Jonsson, The long-term corrosion behavior of FeCrAl(Si) alloys after breakaway oxidation at 600 °C, Corros. Sci. 217 (2023) 111155.
[16] V. Ssenteza, J. Eklund, S. Bigdeli, T. Jonsson, Long-term corrosion behavior of FeCr(Al, Ni) alloys in O2 + H2O with KCl(s) at 600 ° C: Microstructural evolution after breakaway oxidation, Corros. Sci. 226 (2024) 111654.
[17] J. Eklund, A. Persdotter, I. Hanif, S. Bigdeli, T. Jonsson, Secondary corrosion protection of FeCr(Al) model alloys at 600 ° C – The influence of Cr and Al after breakaway corrosion, Corros. Sci. 189 (May) (2021) 109584.
[18] A. Persdotter, Beyond Breakaway Corrosion: Investigating the Secondary Corrosion Protection of Iron-Based Alloys (Doctoral thesis), Chalmers University of Technology, 2023, https://research.chalmers.se/en/publication/537954.
[19] A.N. Hansson, M. Montgomery, M.A.J. Somers, Development of the inner oxide zone upon steam oxidation of an austenitic stainless steel, Mater. High Temp. 26 (1) (2009) 39–44.
[20] J. Eklund, B. Jönsson, A. Persdotter, J. Liske, J. Svensson, T. Jonsson, The influence of silicon on the corrosion properties of FeCrAl model alloys in oxidizing environments at 600 °C, Corros. Sci. 144 (2018) 266–276.
[21] J.O. Andersson, T. Helander, L. Höglund, P.F. Shi, B. Sundman, Thermo-Calc and DICTRA, Computational tools for materials science, CALPHAD 26 (2002) 273–312.
[22] A. La Fontaine, H.W. Yen, P.J. Felfer, S.P. Ringer, J.M. Cairney, Atom probe study of chromium oxide spinels formed during intergranular corrosion, Scr. Mater. 99 (2015) 1–4.
[23] J. Eklund, I. Hanif, S. Bigdeli, T. Jonsson, High temperature corrosion behavior of FeCrAlSi model alloys in the presence of water vapor and KCl at 600 ° C – The influence of Cr content, Corros. Sci. 198 (2022).
[24] S.-H. Kim, S. Bhatt, D.K. Schreiber, J. Neugebauer, C. Freysoldt, B. Gault, S. Katnagallu, Understanding atom probe's analytical performance for iron oxides using correlation histograms and ab initio calculations, New J. Phys. 26 (033021) (2024).
[25] T. Jonsson, B. Pujilaksono, H. Heidari, F. Liu, J.-E. Svensson, M. Halvarsson, L.-G. Johansson, Oxidation of Fe-10Cr in O_2 and in O_2+H_2O environment at 600 °C: A microstructural investigation, Corros. Sci. 75 (2013) 326–336.
[26] A. Persdotter, H. Larsson, J. Eklund, S. Bigdeli, T. Jonsson, The influence of Nickel on the corrosion protection of FeCrNi alloys after breakaway corrosion at 600 °C. Unpublished.